

EFFECT OF DEFORMATION TECHNIQUE ON MECHANICAL PROPERTIES AND AGING BEHAVIOR OF AN Al ALLOY

*I. Zuiko and R. Kaibyshev

*Belgorod State University
Belgorod, Russia*

(*Corresponding author: zuiko_ivan@bsu.edu.ru)

ABSTRACT

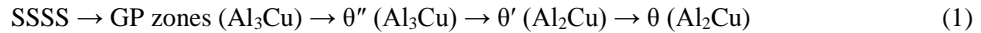
The effect of thermomechanical processing (TMP) including cold working by tension or rolling before aging on mechanical properties and a dispersion of secondary phase particles of an AA2519 alloy (Al-5.64Cu-0.33Mn-0.23Mg-0.15Zr-0.11Ti-0.09V-0.08Fe-0.01Si (wt. %)) was examined. It was shown that the use of tension to impart pre-strain $\leq 10\%$ in the alloy provides the best combination of properties in peak aging condition of the material. The AA2519T87 alloy processed by tension exhibits the yield stress, ultimate tensile strength and elongation to failure of 425.4 ± 2.4 , 475 ± 2.4 , 12.1 ± 0.4 , respectively. The one pass rolling leads to -5% decreases in yield stress and -20% decreases in ductility. Dislocations serve as heterogeneous nucleation sites for θ' -phase precipitation. The positive effect of tension is attributed to the formation of more homogeneous dislocation structure, uniform distribution of θ' -phase particles with higher aspect ratio. Precipitation of the Ω -phase plates on $\{111\}_\alpha$ habit plane was detected. In addition it was shown that the low angle boundaries are heterogeneous nucleation sites for θ' and Ω particles.

KEYWORDS

Aluminum alloys, Thermomechanical processing, Mechanical properties, Microstructure, Precipitation

INTRODUCTION

Precipitation-hardened alloys are a commercially important group of the materials because their mechanical properties can be modified by treating and changing the microstructure. Age-hardenable aluminum alloys belonging to the Al–Cu–Mg system are widely used due to their attractive combination of high specific strength, good fracture toughness and enhanced creep resistance attributed to the highly efficient strengthening by the θ' -phase (Palmer, StJohn, Nie, & Qian, 2017). An AA2519 alloy exhibiting superior mechanical properties among high-strength Al–Cu alloys (2XXX-serie) due to minor Mg additives. It is known that, in alloys with high Cu/Mg ratio (≥ 5.6) the classic precipitation sequence (Palmer et al., 2017; Wang & Starink, 2005; Wang et al., 2010) of supersaturated solid solution (SSSS) decomposition occurs:



Usually sheets from AA2519 alloy are produced through T87 TMP which includes three subsequent operations: solution heat treatment followed by quenching, cold working with a strain of $\sim 7\%$ and subsequent peak aging (Palmer et al., 2017; Wang et al., 2010; Zuiko, Gazizov, & Kaibyshev, 2016). Small amounts of cold plastic deformation prior to ageing are known to enhance age hardening in overwhelming majority of wrought aluminium alloys. This fact attributed with increased density of crystal defects, which act as preferential matrix nucleation and growth sites. In particular high strength and sufficient ductility of Al–Cu–Mg alloys is provided by a dispersion of θ' -phase nucleated on dislocations (Palmer et al., 2017; Wang & Starink, 2005; Wang et al., 2010; Zuiko et al., 2016). In practice of metallurgical work the intermediate strain is conventionally imposed in the sheet by rolling (Palmer et al., 2017). However, in practice of aerospace industry this strain has to be imposed by stretching for articles having complex shape. There is no information on effect of deformation technique on distribution of secondary phase particles and mechanical properties of an AA2519 alloy. So in this contribution we directly compare mechanical properties and a dispersion of secondary phases evolved after T87 with a 7% strain imposed by tension and rolling. The results may be useful for implementation of AA2519T87 for the fabrication of large-scale articles.

EXPERIMENTAL PROCEDURE

An AA2519 alloy was prepared by semi-continuous casting followed by homogenization annealing at 510°C for 24 h. The nominal chemical composition of the alloy was defined via optical emission spectrometer FOUNDRY-MASTER UVR and given in Table 1.

Table 1. Chemical composition of aluminium alloy AA2519

Cu	Mn	Mg	Zr	Ti	V	Zn	Fe	Sn	Ni	Si	Al
5.64	0.33	0.23	0.15	0.11	0.09	0.08	0.08	0.04	0.02	0.01	balance

Next, the ingots were forged in isothermal conditions at $\sim 400^\circ\text{C}$ along principal axes with rotation by 90° . The total true strain (ε) imposed to ingot was ~ 1.2 . Plates with a 25 mm width, a 70 mm length and a 3.22 mm thickness (dictated by the rolling reduction) were machined from central parts of forged billets. The plates were solution treated at 525°C for 1 h and immediately quenched in cold water. Then plates were handled to small amount of plastic deformation at room temperature by 7% rolling in one pass or 7% pre-stretching. True strain imposed by rolling and tension in the AA2519 alloy was the same. The final step was 1.5 h ageing at $190 \pm 1^\circ\text{C}$ (correspond to peak ageing condition). To interrupt decomposition process the plates were quenched in cold ($\sim 20^\circ\text{C}$) water bath. The temper conditions with pre-straining imposed by cold rolling and tension were designated as T87_R and T87_T, respectively. Dog bone specimens with a 25 mm gauge length and a $3 \times 7 \text{ mm}^2$ cross section were machined from the plates using wire electric discharge machine Sodick AQ300L. Tension of specimens to failure (as well as pre-stretching of plates) at room temperature was carried out at ambient temperature using an Instron 5882 testing machine equipped with automatic high-resolution contacting extensometer MFX 500. Velocity of cross-head is corresponded to an initial strain rate of $1.3 \times 10^{-3} \text{ s}^{-1}$. The yield strength (σ_{YS}) is defined as the

amount of stress that will result in a plastic strain of 0.2%. The values of the strength and ductility were averaged and rounded over tests of three samples at each experimental point.

Microhardness measurements were performed using a Wolpert 402-MVD tester at room temperature on mechanically with diamond slurry followed by electrically polished mirror-finish surfaces using a 2 N load and dwell time 10 sec. A value is based on a series of 12 indentations. The maximum and minimum values were discarded and the average of the remaining 10 readings was used.

Longitudinal section (containing the stretching/rolling and the normal directions) was chosen for examination as the best section to reveal microstructural features. The thin foils were electropolished in a solution of 25% nitric acid and 75% methanol at -30°C using a Tenupol-5 twin-jet polishing unit for transmission electron microscopy (TEM). TEM studies were performed using a JEOL JEM-2100 microscope and a FEI TECNAI-G² microscope with a double-tilt stage and a field emission gun operated at 200 kV. The diameter and thickness of the θ' -phase plates were measured from TEM images with in zone axis of $\langle 001 \rangle_{\alpha}$ the aluminum matrix. The BF-image observed in the $\langle 001 \rangle_{\alpha}$ zone axis makes visible of two variants (from three) of such precipitates with $\{001\}_{\alpha}$ habit plane as GP-zones, θ'' -, θ' -phase while the third variant is almost invisible. The $\langle 011 \rangle_{\alpha}$ foil orientation shows three sets of edge-on precipitates, one set (of the three) with a $\{001\}_{\alpha}$ habit plane and the two variant of plates with $\{111\}_{\alpha}$ habit plane. Approximately 500 measurements of the plate dimensions for each condition were performed using at least ten arbitrarily selected typical TEM images for each data point. Misorientations were calculated by the Kikuchi line technique. Other details of techniques for examination of distribution of secondary phase particles were described in previous works (Zuiko & Kaibyshev, 2017; Zuiko et al., 2016).

RESULTS AND DISCUSSION

Tensile properties are summarized in Figure 1. It is seen that pre-straining technique affects yielding. Discontinuous yielding is observed after tension whereas the rolled alloy exhibits continuous yielding. As a result, ultimate tensile strength and microhardness of 156 ± 3 and 157 ± 3 $\text{HV}_{0.2}$ for T87_R and T87_T conditions, respectively, are nearly the same. Yield stress is higher for pre-tensioned alloy. In addition, this material condition exhibits higher elongation-to-failure due to prolonged necking after ultimate stress. It is worth noting that microhardness of the AA2519 alloy in quenched condition is 96 ± 1 $\text{HV}_{0.2}$ and 131 ± 4 $\text{HV}_{0.2}$ after aging at 190°C for 1.5 h without pre-straining. Therefore, pre-straining provides significant increase in strength.

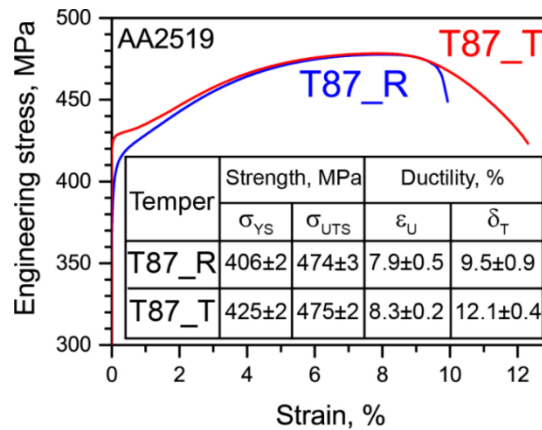


Figure 1. Typical engineering stress-strain curves for peak aged AA2519T87 alloy after rolling (T87_R) and tension (T87_T). σ_{YS} , σ_{UTS} , ϵ_U and δ_T are denoted the yield stress, ultimate tensile strength, uniform elongation and elongation-to-failure, respectively.

The areas of $500 \times 500 \mu\text{m}$ with step of $1 \mu\text{m}$ from the center (in order to avoid surface effect) of specimens were scanned and presented in Figure 2. Mixed network of low- and high-angle boundaries is observed after pre-straining. The average grain sizes are nearly the same: ~ 15 and $\sim 18 \mu\text{m}$ after rolling and tension, respectively. Cold rolling provides slightly increased portion of HABs and density of lattice dislocations (Table 2). It is seen that pre-straining by tension or cold rolling provides increase in lattice dislocation densities by factors 12 and 16, respectively. However, TEM has shown (not presented in this communication) that distribution of lattice dislocations is more uniform after tension.

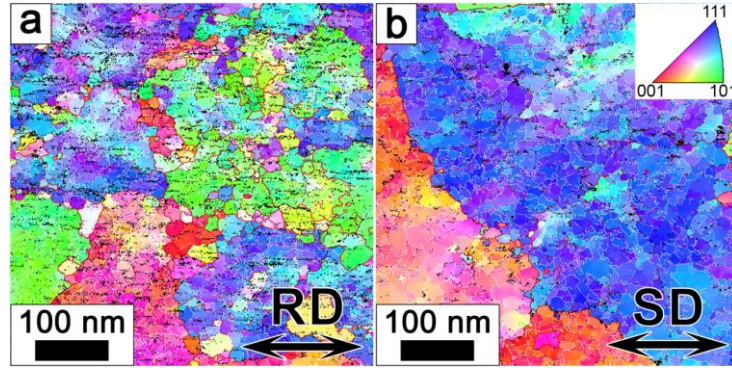


Figure 2. Representative EBSD-maps of AA2519 structure after solution treatment and a) rolling and b) pre-stretching. The low-angle boundaries (LABs) ($2^\circ < \theta < 15^\circ$) and high angle boundaries (HABs) ($\theta \geq 15^\circ$) were depicted as white and red lines, respectively. The OIM data points with confidence index below 0.1 were replaced by black dots and weren't taken into account. The inverse pole figure is shown for the deformation direction. RD and SD are means rolling and pre-stretching direction, respectively. The triangle in upper-right corner of figure b) correlates each color in the maps with a specific grain orientation.

Table 2. Evolution of the dislocation density measured *via* XRD in AA2519 after rolling and tension.

State	ρ_d, m^{-2}
solution treatment	$4.56 \pm 0.96 \times 10^{13}$
solution treatment + 7% rolling	$5.59 \pm 1.09 \times 10^{14}$
solution treatment + 7% tension	$7.18 \pm 2.10 \times 10^{14}$

As mentioned above, the final step in T87 temper consists of artificial aging (at 190°C in our case) with an objective to obtain a dispersion of fine metastable nano-scale precipitates. The identification of the hardening precipitation we performed with the help of the diffraction patterns. Figures 3 and 4 present the experimental and simulated selected area diffraction patterns (SAED). Following careful examination the next features could be revealed:

1. The $\langle 100 \rangle_\alpha$ streaks through $\{200\}_\alpha$ position exhibits pronounced maxima at $\{100\}_\alpha$ (so-called "discontinuous streaks") are observed concurrently with spots reflections at the $\{110\}_{\text{Al}}$ positions from the precipitates whose broad faces lie perpendicular to the beam (Gazizov & Kaibyshev, 2015; Murray, 1985; Phillips, 1975; Ringer, Hono, Polmear, & Sakurai, 1996; Wang & Starink, 2005). This is manifestation of θ'' -phase precipitation (Murray, 1985; Phillips, 1975; Ringer et al., 1996; Wang & Starink, 2005);
2. Spots at the $\{110\}_\alpha$ positions from the platelets lying in the plane of the foil and normal to the beam direction are observed. The shortened four streaks which are immediately adjacent and developed strong maxima corresponding to the $\{110\}_\alpha$ positions. Therefore, θ' -phase precipitated (Murray, 1985; Wang & Starink, 2005);
3. A set of reflections at $1/3$ and $2/3g = \{022\}_\alpha$ as well as $\{111\}_\alpha$ diffuse striking in corresponding $\langle 011 \rangle_\alpha$ SAED pattern. This is indicative for precipitation of Ω -phase (Gazizov & Kaibyshev, 2015; Wang & Starink, 2005; Zuiko et al., 2016). It should be noted that the intense streaks which are visible on the $\langle 011 \rangle_\alpha$, is indicative for very thin plates having a high aspect ratio.

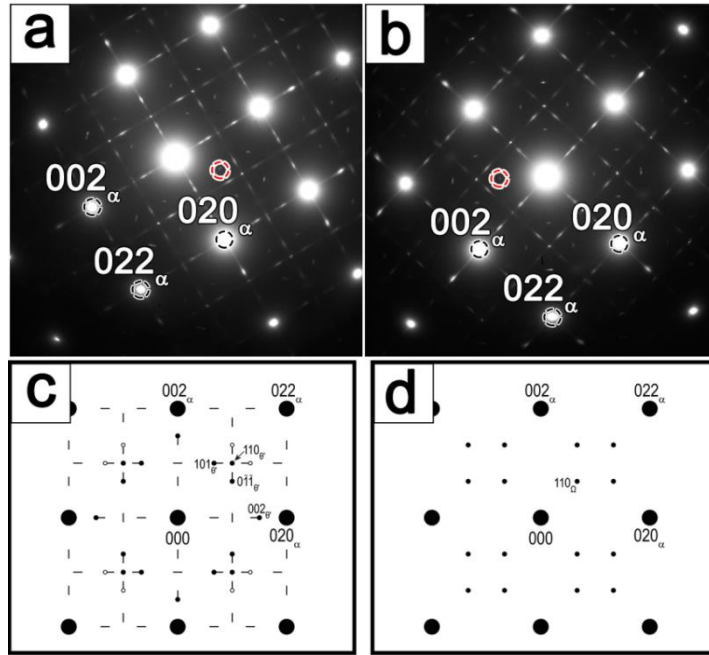


Figure 3. Diffraction patterns in the T87_R (a) and T87_T (b) conditions in the $[001]_{\alpha}$ zone axis. (c) and (d) are indexed schemes of experimental electron diffraction patterns. Red circles mark reflexes from Ω phase. The a) and b) patterns correspond to Figures 6a and 6c, respectively. For the sake of distinct and effective comparison of diffuse-diffracted intensity, the SAED patterns we recorded using the same aperture (size of $1.4 \mu\text{m}$) and electron beam intensity (minimum).

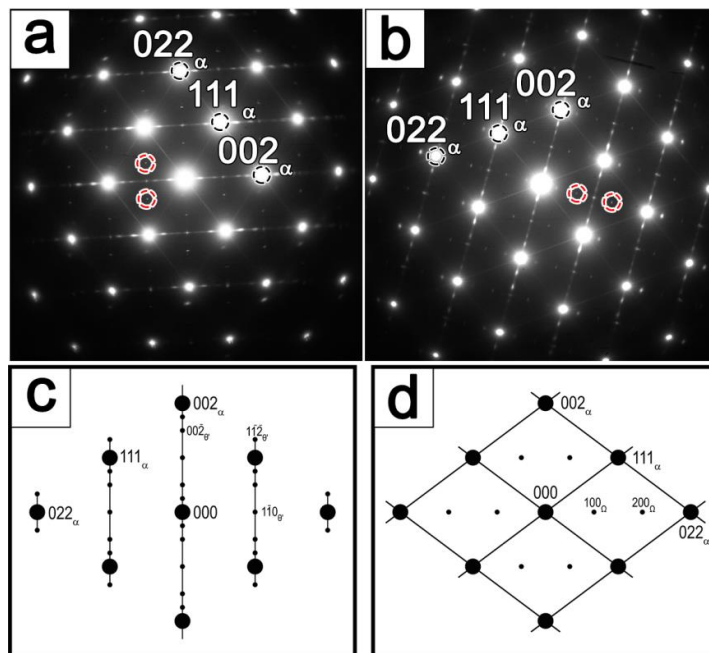


Figure 4. Experimental: in the T87_R (a), T87_T (b) conditions and schematic (c, d) electron diffraction patterns for zone axis $[011]_{\alpha}$. Red circles denote reflexes from Ω phase. The a) and b) patterns correspond to Figures 7a and 7b, respectively.

TEM bright-field (BF) and correspond dark-field (DF) images are presented in Figure 5. Precipitations having plate-like shape and the $\{100\}_\alpha$ habit plane are observed. The DF-images obtained using the $\{011\}_\alpha$ forbidden reflections show edge-on two variants of θ' -phase (Figures 5b and 5d). So, BF-images show an evidence for the co-existence of θ'' - and θ' -phases. The key plate dimensions are summarized in Table 3. Concurrent inspection of BF and DF images (Figure 5) shows that number density of θ'' -phase after rolling is slightly higher than that after stretching whereas number density of the θ' -phase is higher after pre-straining by tension. In addition, last technique provides more uniform distribution of θ' -phase platelets with higher aspect ratio that leads to increased yield stress (da Costa Teixeira et al., 2008; Nie & Muddle, 2008).

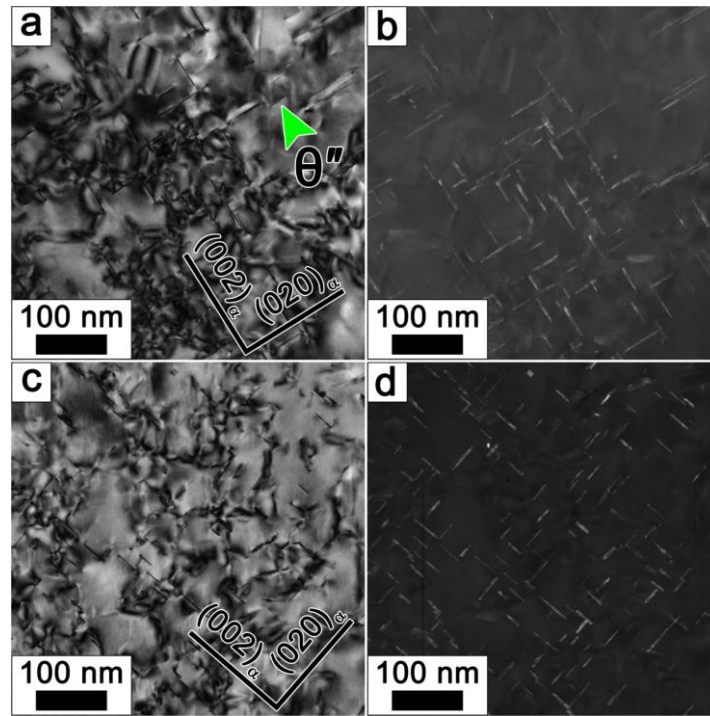


Figure 5. DF-TEM-images (b, d) was taken from the same (a, b) places using $\{011\}_\alpha$ reflection. More uniform distribution of θ' -precipitates is clearly seen in micrograph d. Note the coherence-strain fields of θ'' -precipitates (marked with green arrow) caused by the misfit perpendicular to the plates.

Table 3. Effect of pre-strain technique on the mean precipitate sizes of the main strengthening agents within the grain/subgrain interiors of AA2519. The experimental errors of measurements are listed based on the particle size distribution (as standard deviation).

Temper	Phase	Plate diameter, nm	Plate thickness, nm	Aspect ratio
T87_R	θ'	36.4 ± 15.0	1.89 ± 0.54	19.2
	Ω	31.5 ± 12.6	0.71 ± 0.19	44.3
T87_T	θ'	25.9 ± 10.5	2.55 ± 0.71	10.1
	Ω	36.6 ± 14.4	0.99 ± 0.19	37.2

BF-TEM micrographs taken near $\langle 011 \rangle_\alpha$ zone axis are presented in Figure 6. It is seen that two types of precipitates having plate-like shape with $\{001\}_\alpha$ (θ''/θ' -phases) and $\{111\}_\alpha$ (Ω -phase) habit planes edge-on to the electron beam. The diameter and aspect ratio of the Ω -phase plates are higher in comparison with the same characteristics of θ''/θ' -phases particles (Table 3). Contrast near plates is indicative for the presence of large coherent stress at the Ω -phase plates.

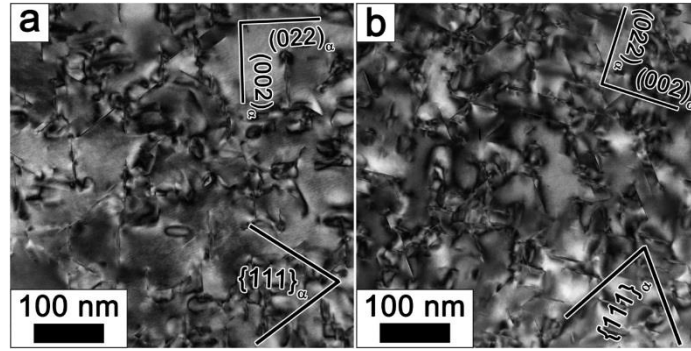


Figure 6. Bright-field TEM images of the microstructure after 7% ($\epsilon \sim 0.07$) pre-strain using rolling (a), (b) tension and peak aging (190°C for 1.5 h). From images it is straightforward to identify the presence of the θ''/θ' and Ω -phases. Note that the last was distributed uniformly through the matrix.

During TEM experiments we have noticed that several plates of θ' and Ω -phases located on boundaries. The examples of such heterogeneously precipitated both strengthening agents are given at Figure 7. The specific contrast on both sides of boundary testifies that crystal lattice was rotated. The misorientation angles pictured on Figures 7a and 7b are 1.2° and 7.5° , respectively. Boundary θ' -phase particles exhibit a large thickness of $\sim 8\text{--}9$ nm and a very low aspect ratio of ~ 4 . In contrast, dimensions of boundary Ω -phase particles and particles of this phase located in Al matrix are nearly the same. The boundary Ω -phase plates exhibit predominant orientations close to the $\{111\}_\alpha$ plane.

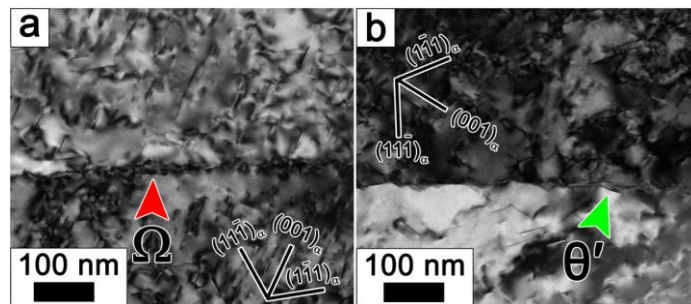


Figure 7. Bright-field TEM images showing plate-shaped boundary precipitation in AA2519T87. Red and green arrows indicate plates of Ω and θ' -phase, respectively. Images taken near the $[011]_\alpha$ zone axis.

We demonstrated that tension provides more uniform distribution of dislocations and, therefore, plates of θ' -phase nucleated at them. In addition, aspect ratio of θ' -phase increases. Distribution of θ' -platelets strongly affects propagation of Lüders bands (Yuzbekova et al., 2017). Homogeneous distribution of θ' -platelets with a high diameter and aspect ratio provides discontinuous yielding that is the main reason for increased values of yield stress after tension. In addition, this distribution affects necking (Yuzbekova et al., 2017) providing increased ductility. Herewith, no effect of θ' -platelets distribution on ultimate tensile strength and microhardness takes place. Stretching is viable for fabrication of articles from AA2519 alloy with increased yield stress and elongation-to-failure.

CONCLUSIONS

- 1) Pre-straining by tension provides increased yield stress due to transition from continuous yielding to discontinuous one and increased ductility. No effect of pre-straining technique on ultimate tensile strength and microhardness was registered.
- 2) Pre-straining by tension provides more uniform distribution of dislocations and lower dislocation density. This dislocation structure provides precipitation of θ' -phase particles with increased diameter and aspect ratio. In addition, number density of θ'' -phase particles decreases.

- 3) Precipitation of Ω -phase with a high aspect ratio takes place.
- 4) The heterogeneous nucleation of both Ω and θ' -phases on low-angle boundaries was demonstrated.

ACKNOWLEDGMENTS

This work is supported by the Ministry of Education and Science of the Russian Federation under the agreement №14.584.21.0023. The authors are grateful to the staff of the Joint Research Center, «Technology and Materials» Belgorod State National Research University for their assistance with the mechanical and structural characterizations.

REFERENCES

- da Costa Teixeira, J., Cram, D. G., Bourgeois, L., Bastow, T. J., Hill, A. J., & Hutchinson, C. R. (2008). On the strengthening response of aluminum alloys containing shear-resistant plate-shaped precipitates. *Acta Materialia*, 56(20), 6109–6122. <https://doi.org/10.1016/j.actamat.2008.08.023>
- Gazizov, M., & Kaibyshev, R. (2015). Effect of pre-straining on the aging behavior and mechanical properties of an Al–Cu–Mg–Ag alloy. *Materials Science and Engineering: A*, 625, 119–130. <https://doi.org/10.1016/j.msea.2014.11.094>
- Murray, J. L. (1985). The aluminium-copper system. *International Metals Reviews*, 30(1), 211–234. <https://doi.org/10.1179/imtr.1985.30.1.211>
- Nie, J. F., & Muddle, B. C. (2008). Strengthening of an Al–Cu–Sn alloy by deformation-resistant precipitate plates. *Acta Materialia*, 56(14), 3490–3501. <https://doi.org/10.1016/j.actamat.2008.03.028>
- Palmer, I., StJohn, D., Nie, J.-F., & Qian, M. (2017). *Light Alloys 5th Edition: Metallurgy of the Light Metals* (5th ed.). Butterworth-Heinemann. <https://www.elsevier.com/books/light-alloys/polmear/978-0-08-099431-4>
- Phillips, V. A. (1975). High resolution electron microscope observations on precipitation in Al-3.0% Cu alloy. *Acta Metallurgica*, 23(6), 751–767. [https://doi.org/10.1016/0001-6160\(75\)90058-9](https://doi.org/10.1016/0001-6160(75)90058-9)
- Ringer, S. P., Hono, K., Polmear, I. J., & Sakurai, T. (1996). Nucleation of precipitates in aged Al-Cu-Mg-(Ag) alloys with high Cu:Mg ratios. *Acta Materialia*, 44(5), 1883–1898. [https://doi.org/10.1016/1359-6454\(95\)00314-2](https://doi.org/10.1016/1359-6454(95)00314-2)
- Wang, S. C., & Starink, M. J. (2005). Precipitates and intermetallic phases in precipitation hardening Al–Cu–Mg–(Li) based alloys. *International Materials Reviews*, 50(4), 193–215. <https://doi.org/10.1179/174328005X14357>
- Wang, W., Zhang, X., Gao, Z., Jia, Y., Ye, L., Zheng, D., & Liu, L. (2010). Influences of Ce addition on the microstructures and mechanical properties of 2519A aluminum alloy plate. *Journal of Alloys and Compounds*, 491(1–2), 366–371. <https://doi.org/10.1016/j.jallcom.2009.10.185>
- Yuzbekova, D., Mogucheva, A., Zhemchuzhnikova, D., Lebedkina, T., Lebyodkin, M., & Kaibyshev, R. (2017). Effect of microstructure on continuous propagation of the Portevin-Le Chatelier deformation bands. *International Journal of Plasticity*, 96, 210–226. <https://doi.org/10.1016/j.ijplas.2017.05.004>
- Zuiko, I., & Kaibyshev, R. (2017). Deformation structures and strengthening mechanisms in an Al-Cu alloy subjected to extensive cold rolling. *Materials Science and Engineering A*, 702. <https://doi.org/10.1016/j.msea.2017.07.001>
- Zuiko, I. S., Gazizov, M. R., & Kaibyshev, R. O. (2016). Effect of thermomechanical treatment on the microstructure, phase composition, and mechanical properties of Al–Cu–Mn–Mg–Zr alloy. *The Physics of Metals and Metallography*, 117(9), 906–919. <https://doi.org/10.1134/S0031918X16090088>